
RELATIONS BETWEEN DEFLECTIONS AND LOAD: FROM KIRCHHOFF THIN PLATE TO REISSNER-MINDLIN THICK PLATE

TECHNICAL REPORT

Qianyu Chen

School of Information Science and Technology
ShanghaiTech University
chenqy1@shanghaitech.edu.cn

Mokai Pan

School of Information Science and Technology
ShanghaiTech University
panmk@shanghaitech.edu.cn

Yu Shi

School of Information Science and Technology
ShanghaiTech University
shiyu1@shanghaitech.edu.cn

June 19, 2024

ABSTRACT

The thin plate bending problem based on Kirchhoff theory is the most common and basic problems in plate structure, mathematically modelled as edge-value problems with fourth-order partial differential equations. In order to solve this high-order partial differential equation problem, we take two methods: finite difference method and finite element analysis for solving thin plate bending problem. With two methods, the MSE error between our solution and the exact solution is reduced to 10^{-4} . For more comparison, We take the method of finite element analysis with Reissner-Mindlin theory for solving thick plate bending problem to explore the deflections on both thin and thick plates with the same load. During the experiments, we found a phenomenon called shear locking and did some in-depth research about it and studied the solution of eliminating this effect. Furthermore, we made some extension research about modal analysis.

Keywords Deflection · Kirchhoff plate · Reissner-Mindlin plate · Finite difference method · Finite element analysis

1 Introduction

Plate is a very important basic structure in practical engineering, it is widely used in bridges, shipbuilding, metallurgy, vehicles and other engineering fields. The plate and shell structure analysis originates in the 18th century. Euler was the first to explore the bending problem of plates. In 1850, Kirchhoff provided the first complete theory of thin plate bending. Subsequently, Aron (1874) conducted analytical work on thin shells. In 1945, Reissner relaxed Kirchhoff's assumptions by considering the effects of transverse shear deformation, thus making it applicable to moderately thick plates and shells. Later, Mindlin (1951) also relaxed the same assumptions in a different manner. Tang et al. [2018]

Among several classical assumptions introduced for calculating plate and shell elements before solid elements were feasible, the two most common theories are based on the Kirchhoff and the Reissner-Mindlin assumptions. The problem of solving plate structures is essentially about solving boundary value problems for higher-order partial differential equations. Direct analytical solutions to these problems are extremely challenging from a mathematical standpoint. In practical engineering, plate structure problems often involve more complex boundary conditions, making analytical solutions for such problems highly valuable both in terms of practical applications and theoretical significance.

With the development of computers, numerical computation has received more and more attention. In this paper, we will briefly introduce finite difference method (MITCHELL and Griffiths [1980]) on thin plates, the finite element analysis (Sudhir [2012]) on both thin and thick plates and the related shear locking phenomenon and modal analysis on thin plates.

2 Physician Modelling

2.1 Thin plates: Kirchhoff theory

2.1.1 Assumptions

A plate is defined as a flat solid whose thickness is much smaller than its other dimensions. We assume that the middle plane is equidistant from the upper and lower faces. This plane is taken as the reference plane ($z = 0$) for deriving the plane kinematic equations. Oñate [2013a]

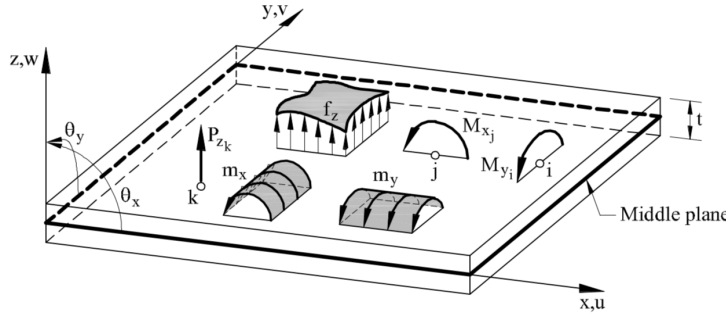


Figure 1: Geometric definition of a plate.

The classical thin plate theory based is on Kirchhoff's assumption, which ignores the effect of shear deformation.

And the assumptions of Kirchhoff thin plate theory are as follows:

1. In the points belonging to the middle plane ($z = 0$): $u = v = 0$. Namely, the points on the middle plane only move vertically.
2. The points along a normal to the middle plane have the same vertical displacement (i.e. the thickness does not change during deformation).
3. The normal stress σ_z is negligible (plane stress assumption).
4. A straight line normal to the undeformed middle plane remains straight and normal to the deformed middle plane(normal orthogonality condition).

where Assumptions 1, 2 and 4 allow the displacement field to be defined over the whole plate. Assumption 3 affects the stress-strain relationship.

2.1.2 Partial Differential Equation Derivation

Based on the Kirchhoff assumption 4, which implies:

$$\gamma_{xz} = \gamma_{yz} = 0 \quad (2-1-1)$$

from geometry equation,

$$\frac{\partial U}{\partial z} = -\frac{\partial W}{\partial x}, \frac{\partial V}{\partial z} = -\frac{\partial W}{\partial y} \quad (2-1-2)$$

and W has nothing to do with z

$$W = W(x, y) \quad (2-1-3)$$

Integrate on Eq 2-1-2, we get

$$U = -z \frac{\partial W}{\partial x}, \quad V = -z \frac{\partial W}{\partial y} \quad (2-1-4)$$

We denote each strain component by W . According to the physical equations and Hooke's law, we obtain each stress component expressed by the deflection W

$$\sigma_x = -\frac{Ez}{1-\mu^2} \left(\frac{\partial^2 W}{\partial x^2} + \mu \frac{\partial^2 W}{\partial y^2} \right), \quad \sigma_y = -\frac{Ez}{1-\mu^2} \left(\frac{\partial^2 W}{\partial y^2} + \mu \frac{\partial^2 W}{\partial x^2} \right), \quad \sigma_{xy} = -2Gz \frac{\partial^2 W}{\partial x \partial y} \quad (2-1-5)$$

Due to the deflection W being an even function of x, y and independent of z , the stress components σ_x, σ_y , and τ_{xy} are proportional and linearly distributed along the thickness direction. Based on the The straight normal assumption, $\tau_{yz} = \tau_{xz} = 0$, we have

$$\frac{\partial \tau_{zx}}{\partial z} = -\frac{\partial \sigma_x}{\partial x} - \frac{\partial \tau_{yx}}{\partial y}, \frac{\partial \tau_{zy}}{\partial z} = -\frac{\partial \sigma_y}{\partial y} - \frac{\partial \tau_{xy}}{\partial x} \quad (2-1-6)$$

Due to the Shear stress reciprocity theorem, $\tau_{yx} = \tau_{xy}$, and the boundary conditions on the upper and lower surfaces of thin plates: $\tau_{zx}|_{z=\pm\frac{h}{2}} = 0, \tau_{zy}|_{z=\pm\frac{h}{2}} = 0$, we can have

$$\tau_{zx} = \frac{E}{2(1-\mu^2)} \left(z^2 - \frac{h^2}{4} \right) \frac{\partial}{\partial x} \nabla^4 W, \tau_{zy} = \frac{E}{2(1-\mu^2)} \left(z^2 - \frac{h^2}{4} \right) \frac{\partial}{\partial y} \nabla^4 W \quad (2-1-7)$$

From Eq 2-1-7, it can be seen that the vertical shear stresses τ_{zx} and τ_{zy} are distributed in a parabolic pattern along the thickness direction of the thin plate. Similarly σ_z can be calculated from the equilibrium equations of plate microcellular,

$$\frac{\partial \tau_{xz}}{\partial x} + \frac{\partial \tau_{yz}}{\partial y} + \frac{\partial \sigma_z}{\partial z} = 0 \quad (2-1-8)$$

Substituting equation Eq 2-1-7 into equation Eq 2-1-8, since $\tau_{xz} = \tau_{zx}, \tau_{yz} = \tau_{zy}$, we get

$$\sigma_z = \frac{E}{2(1-\mu^2)} \left(\frac{h^2}{4} - \frac{z^3}{3} \right) \nabla^4 W \quad (2-1-9)$$

Therefore, we obtain

$$\sigma_z = \frac{E}{2(1-\mu^2)} \left(\frac{h^2}{4} - \frac{z^2}{3} - \frac{h^2}{12} \right) \nabla^4 W = -\frac{Eh^3}{6(1-\mu^2)} \left(\frac{1}{2} - \frac{z}{h} \right)^2 \left(1 + \frac{z}{h} \right) \nabla^4 W \quad (2-1-10)$$

Substituting Eq 2-1-10 into the boundary condition $q = \sigma_z|_{z=\frac{h}{2}}$, where q is the transverse load per unit area on the plate, we get

$$D \nabla^4 W = q(x, y) \quad (2-1-11)$$

In conclusion, we get the the deflection $w(x, y)$ of the plate satisfies the following partial differential equation based on Kirchhoff plate theory in which $q(x, y)$ is the distributed load, also:

$$D = \frac{Eh^3}{12(1-\nu^2)}$$

D is the flexural rigidity, E is the Young's modulus, h is the thickness, and ν is the Poisson's ratio. Oñate [2013a]

2.2 Thick plates: Reissner-Mindlin Theory

2.2.1 Assumptions

A fundamental consideration in the analysis of plate bending problems is the distinction between thick and thin plate formulations. The varying thicknesses of plates necessitate the application of different theoretical approaches to accurately analyze their bending behavior. In cases involving thick plate bending, the Reissner-Mindlin plate theory is employed and we'll follow up with more details on what it's all about. Oñate [2013b]

The Mindlin theory is a first-order shear deformation plate theory, which gives good results for moderately thick plates. Reissner-Mindlin plate theory assumes that the normals to the plate do not remain orthogonal to the mid-plane after deformation, thus allowing for transverse shear deformation effects.

Reissner-Mindlin plate bending theory shares the first three assumptions of Kirchhoff plate theory 2.1. The fourth assumption on the rotation of the normal is different and reads as follows:

4. A straight line normal to the undeformed middle plane remains straight but not necessarily orthogonal to the middle plane after deformation

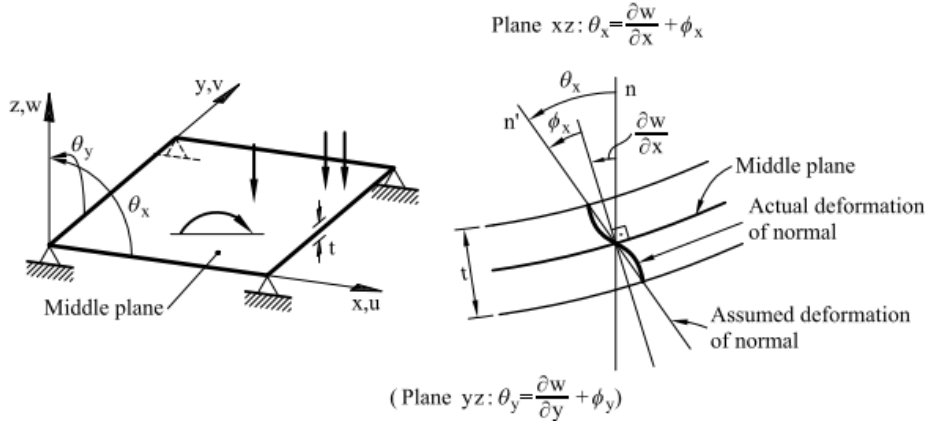


Figure 2: Reissner-Mindlin plate theory.

2.2.2 Displacement Field

Based on the Reissner-Mindlin Theory and thick plate foundation formulation, let's start by observing the 3D displacement field which is expressed in terms of the middle plane kinematic variables w , θ_x and θ_y as

$$u(x, y, z) = -z\theta_x(x, y), v(x, y, z) = -z\theta_y(x, y), w(x, y, z) = w(x, y) \quad (2-2-1)$$

where θ_x and θ_y are the angles defining the rotation of the normal vector. Eq 2-2-1 is identical to the 3D displacement field for Kirchhoff theory. Here again the middle plane is taken as the reference plane($z = 0$). According to the assumption 4, we can express the rotation of the normal on the plane xz and yz as

$$\theta_x = \frac{\partial \omega}{\partial x} + \phi_x, \theta_y = \frac{\partial \omega}{\partial y} + \phi_y \quad (2-2-2)$$

The rotation of the normal in each of the two vertical planes xz and yz is obtained as the sum of two terms:

1. the adequate slope of the plate middle plane.
2. an additional rotation ϕ resulting from the lack of orthogonality of the normal with the middle plane after deformation

Then we proceed to express the strain and stress fields of the thick plate. Substituting the displacement field (Eq 2-2-1) into the expression for the strains in a 3D solid gives:

$$\hat{\varepsilon}_b = \begin{Bmatrix} \hat{\varepsilon}_x \\ \hat{\varepsilon}_y \\ \hat{\gamma}_{xy} \end{Bmatrix} = \begin{Bmatrix} \frac{\partial \theta_x}{\partial x} \\ \frac{\partial \theta_y}{\partial y} \\ \left(\frac{\partial \theta_x}{\partial y} + \frac{\partial \theta_y}{\partial x} \right) \end{Bmatrix} \text{ and } \hat{\varepsilon}_s = \begin{Bmatrix} \hat{\gamma}_{xz} \\ \hat{\gamma}_{yz} \end{Bmatrix} = \begin{Bmatrix} \frac{\partial w}{\partial x} - \theta_x \\ \frac{\partial w}{\partial y} - \theta_y \end{Bmatrix} \quad (2-2-3)$$

where vectors ε_b and ε_s contain the bending and transverse shear strains respectively.

Then we can construct the strain vector as:

$$\varepsilon = S\hat{\varepsilon} = S \begin{Bmatrix} \hat{\varepsilon}_b \\ \hat{\varepsilon}_s \end{Bmatrix} = \begin{bmatrix} -z & 0 & 0 & 0 & 0 \\ 0 & -z & 0 & 0 & 0 \\ 0 & 0 & -z & 0 & 0 \\ 0 & 0 & 0 & 1 & 0 \\ 0 & 0 & 0 & 0 & 1 \end{bmatrix} \begin{Bmatrix} \hat{\varepsilon}_b \\ \hat{\varepsilon}_s \end{Bmatrix} \quad (2-2-4)$$

where S is the strain transformation matrix.

In addition to the aforementioned geometrical equations pertinent to thick plates, it is imperative to formulate the physical equations governing stresses and strains. For an orthotropic material, characterized by distinct material properties along three mutually perpendicular axes denoted as 1, 2, and 3 (with axis 3 aligned with the z-direction), these equations can be written as:

$$\sigma_I = \begin{Bmatrix} \sigma_b \\ \sigma_s \end{Bmatrix} = \begin{bmatrix} \hat{D}_b & 0 \\ 0 & \hat{D}_s \end{bmatrix} \begin{Bmatrix} \varepsilon_b \\ \varepsilon_s \end{Bmatrix} = \hat{D}_I \varepsilon_I \quad (2-2-5)$$

where

$$\sigma_b = [\sigma_x, \sigma_y, \tau_{xy}]^T, \quad \sigma_s = [\tau_{xz}, \tau_{yz}]^T, \quad \varepsilon_b = [\varepsilon_x, \varepsilon_y, \gamma_{xy}]^T, \quad \varepsilon_s = [\gamma_{xz}, \gamma_{yz}]^T \quad (2-2-6)$$

are the bending and transverse shear stresses and strains in the principal orthotropy axes and

$$\hat{\mathbf{D}}_b = \frac{E}{1-\mu^2} \begin{bmatrix} 1 & \mu & 0 \\ \mu & 1 & 0 \\ 0 & 0 & \frac{1-\mu}{2} \end{bmatrix}, \quad \hat{\mathbf{D}}_s = \frac{E}{2(1+\mu)} \begin{bmatrix} 1 & 0 \\ 0 & 1 \end{bmatrix} \quad (2-2-7)$$

is the relational stiffness matrix described above, which is used to express the constant maturity of materiality. Additionally, it is imperative to define the vector of resultant stresses at a point in the middle plane of the plate. This vector encapsulates the combined stress components—typically including both normal and shear stresses—at a specific point within the plate's mid-plane. The vector of resultant stresses at a point of the plate middle plane is defined as:

$$\hat{\boldsymbol{\sigma}} = \begin{Bmatrix} \hat{\sigma}_b \\ \dots \\ \hat{\sigma}_s \end{Bmatrix} = \begin{Bmatrix} M_x \\ M_y \\ M_{xy} \\ \dots \\ Q_x \\ Q_y \end{Bmatrix} = \int_{-\frac{t}{2}}^{+\frac{t}{2}} \begin{Bmatrix} -z\sigma_x \\ -z\sigma_y \\ -z\tau_{xy} \\ \dots \\ \tau_{xz} \\ \tau_{yz} \end{Bmatrix} dz = \int_{-\frac{t}{2}}^{+\frac{t}{2}} \begin{Bmatrix} -z\sigma_b \\ \dots \\ \sigma_s \end{Bmatrix} dz = \int_{-\frac{t}{2}}^{+\frac{t}{2}} \mathbf{S}^T \boldsymbol{\sigma} dz \quad (2-2-8)$$

where S is the transformation matrix and vectors $\hat{\sigma}_b$ and $\hat{\sigma}_s$ contain the moments and the shear forces respectively. Besides, we can also calculate the generalized constitutive matrix in Eq 2-2-7 as:

$$\mathbf{D} = \int_{-\frac{t}{2}}^{+\frac{t}{2}} \mathbf{S}^T \hat{\mathbf{D}} \mathbf{S} dz = \int_{-\frac{t}{2}}^{+\frac{t}{2}} \begin{bmatrix} z^2 \hat{\mathbf{D}}_b & \mathbf{0} \\ \mathbf{0} & \hat{\mathbf{D}}_s \end{bmatrix} dz = \begin{bmatrix} \mathbf{D}_b & \mathbf{0} \\ \mathbf{0} & \mathbf{D}_s \end{bmatrix} \quad (2-2-9)$$

After calculation the Eq 2-2-9, we can get the relation between \mathbf{D} and $\hat{\mathbf{D}}$ as:

$$\mathbf{D}_b = \frac{t^3}{12} \hat{\mathbf{D}}_b \quad \text{and} \quad \mathbf{D}_s = t \hat{\mathbf{D}}_s \quad (2-2-10)$$

Based on the aforementioned theoretical framework, we can rigorously analyze the small deflection bending behavior of thick plates by employing both the physical equations governing stresses and strains, as well as the corresponding geometric equations. Shang et al. [2015]

2.3 Boundary Conditions: *ssss* And *cccc* Model

We have considered two models: the simply-supported-rectangular-plate-on-four-sides model (hereinafter referred to as *ssss*) and the clamped-rectangular-plate model (hereinafter referred to as *cccc*). The difference between the two models are boundary conditions: e.g. for the former one, the boundary condition on $x = 0$ is

$$\begin{cases} w(x, y) = 0 \\ \frac{\partial^2 w}{\partial x^2} + \gamma \frac{\partial^2 w}{\partial y^2} = 0 \end{cases} \quad (\textit{ssss})$$

for the latter one, the boundary condition on $x = 0$ is

$$\begin{cases} w(x, y) = 0 \\ \frac{\partial w}{\partial x} = 0 \end{cases} \quad (\textit{cccc})$$

3 Research Methods

3.1 Finite Difference Method

We will choose the *ssss* model to explain in detail about how to apply Finite Difference Method on the model. The goal of the finite difference method is to approximate differential operators by finite difference operators. Tang et al. [2018]

Define the square domain grid as the Figure 3 shows. Assume $N = M$, the left bottom point p_1 has the coordinate $(0,0)$ and the top right point $p_{NM} = p_{N^2}$ has the coordinate $(1,1)$. Define the mesh size h as $h = \frac{1}{N-1}$.

For the point p_k with its coordinate (x_{p_k}, y_{p_k}) on the grid, denote w_k as $w(x_{p_k}, y_{p_k})$ (the deflection value on the point p_k) and q_k as $q(x_{p_k}, y_{p_k})$ (the distributed pressure (load) value on the point p_k)

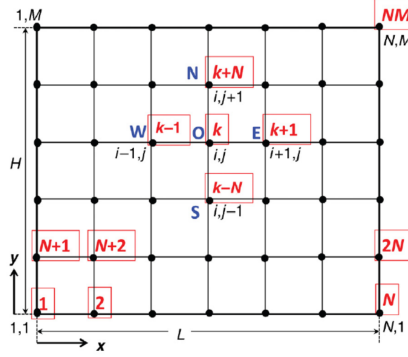


Figure 3: The square domain grid.

We choose centered difference to approximate the higher order partial derivatives at the point $p_{(k-1)N+m}$ (it is located at row k and col m , so k and m satisfies $1 \leq k \leq N$ and $1 \leq m \leq N$ respectively):

$$\frac{\partial^4 w}{\partial x^4} = \frac{1}{h^4} (w_{(k-1)N+m+2} - 4w_{(k-1)N+m+1} + 6w_{(k-1)N+m} - 4w_{(k-1)N+m-1} + w_{(k-1)N+m-2})$$

$$\frac{\partial^4 w}{\partial y^4} = \frac{1}{h^4} (w_{(k+1)N+m} - 4w_{kN+m} + 6w_{(k-1)N+m} - 4w_{(k-2)N+m} + w_{(k-3)N+m})$$

$$\begin{aligned} \frac{\partial^4 w}{\partial x^2 \partial y^2} = & \frac{1}{h^4} (4w_{(k-1)N+m} - 2w_{(k-1)N+m+1} - 2w_{(k-1)N+m-1} - 2w_{kN+m} - 2w_{(k-2)N+m} \\ & + w_{kN+m+1} + w_{kN+m-1} + w_{(k-2)N+m+1} + w_{(k-2)N+m-1}) \end{aligned}$$

Now back to the equations related to the model:

$$\begin{cases} \frac{\partial^4 w}{\partial x^4} + \frac{\partial^4 w}{\partial y^4} + 2\frac{\partial^4 w}{\partial x^2 \partial y^2} = \frac{q(x,y)}{D} & \text{on } (x,y) \in \Omega \\ w(x,y) = 0 & \text{on } (x,y) \in \partial\Omega \\ \frac{\partial^2 w}{\partial x^2} + \gamma \frac{\partial^2 w}{\partial y^2} = 0 & \text{on } (x,y) \in \partial\Omega \end{cases} \quad (3-1-1)$$

We first handle the boundary condition, which is $w(x,y) = 0$ and $\frac{\partial^2 w}{\partial x^2} + \gamma \frac{\partial^2 w}{\partial y^2} = 0$ in the Eq 3-1-1 above.

The finite difference method introduces virtual points outside the control domain when dealing with boundary conditions which will be shown in the following calculations.

As to the points $p_{(k-1)N+m}$ on the boundary, which satisfies $k = 1$ or $k = N$ or $m = 1$ or $m = N$, take the centered difference forms of the points to the equations, we can get:

$$\begin{cases} w_{(k-1)N+m} = 0 \\ \frac{1}{h^2} (w_{(k-1)N+m+1} - 2w_{(k-1)N+m} + w_{(k-1)N+m-1}) + \gamma \frac{1}{h^2} (w_{kN+m} - 2w_{(k-1)N+m} + w_{(k-2)N+m}) = 0 \end{cases}$$

In the case where $k = 1$ or $k = N$, the boundary conditions are equivalent to

$$\begin{cases} w_{(k-1)N+m} = 0 \\ w_{kN+m} + w_{(k-2)N+m} = 0 \end{cases}$$

In the case where $m = 1$ or $m = N$, the boundary conditions are equivalent to

$$\begin{cases} w_{(k-1)N+m} = 0 \\ w_{(k-1)N+m+1} + w_{(k-1)N+m-1} = 0 \end{cases}$$

It may happen that the index may be out of range, for example, for the point satisfies $m = N$, in its boundary conditions, the index of $w_{(k-1)N+m+1}$ is out of range, which is the virtual point outside the control domain we mentioned above. Virtual points are interconnected with the points in the domain and are not additional unknown quantities.

Since on the boundary, we have $w_{(k-1)N+m} = 0$, so we do not need to take Finite Difference Method on them and we mainly care about the points inside.

Before we consider the different situations, we denote some matrix and vectors for brief note.

Denote $A, B_{18}, B_{19}, I, \mathbf{0} \in \mathbb{R}^{(N-2) \times (N-2)}$ and $\mathbf{w}_k, \mathbf{q}_k \in \mathbb{R}^{N-2}$:

$$A = \begin{pmatrix} -8 & 2 & 0 & \cdots & 0 & 0 \\ 2 & -8 & 2 & \cdots & 0 & 0 \\ 0 & 2 & \ddots & \ddots & \vdots & \vdots \\ \vdots & \vdots & \ddots & -8 & 2 & 0 \\ 0 & 0 & \cdots & 2 & -8 & 2 \\ 0 & 0 & \cdots & 0 & 2 & -8 \end{pmatrix} \quad B_{18} = \begin{pmatrix} 18 & -8 & 1 & 0 & 0 & \cdots & 0 & 0 \\ -8 & 19 & -8 & 1 & 0 & \cdots & 0 & 0 \\ 1 & -8 & 19 & -8 & 1 & \cdots & 0 & 0 \\ \vdots & \ddots & \ddots & \ddots & \ddots & \ddots & \vdots & \vdots \\ \vdots & \vdots & \ddots & \ddots & \ddots & \ddots & \ddots & \vdots \\ 0 & 0 & \cdots & 1 & -8 & 19 & -8 & 1 \\ 0 & 0 & \cdots & 0 & 1 & -8 & 19 & -8 \\ 0 & 0 & \cdots & 0 & 0 & 1 & -8 & 18 \end{pmatrix}$$

$$I = \begin{pmatrix} 1 & 0 & \cdots & 0 \\ 0 & 1 & \cdots & 0 \\ \vdots & \vdots & \ddots & \vdots \\ 0 & 0 & \cdots & 1 \end{pmatrix} \quad B_{19} = B_{18} + I$$

$$\mathbf{0} = [0]_{(N-2) \times (N-2)} \quad \mathbf{q}_k = [q_{(k-1)N+2} \quad q_{(k-1)N+3} \quad \cdots \quad q_{kN-1}]^T$$

$$\mathbf{w}_k = [w_{(k-1)N+2} \quad w_{(k-1)N+3} \quad \cdots \quad w_{kN-1}]^T$$

for $k = 2, 3, \dots, N-1$.

Consider the following three situations: points $p_{(k-1)N+m}$ on the $k = 2$ and $N - 1$ row, on the $k = 3$ and $N - 2$ row and on the $4 \leq k \leq N - 3$ row. To be noticed, the third situation is the generalization of the first two situations because the first two are influenced by boundary conditions. So we calculate the third general situation and the first two situations can be calculated similarly.

On k -th row, we would solve the problem in 3 cases:

Case1: point $p_{(k-1)N+2}$:

$$h^4 \nabla^4 w = w_{(k+1)N+2} + 2w_{kN+3} - 8w_{kN+2} + w_{(k-1)N+4} - 8w_{(k-1)N+3} + 19w_{(k-1)N+2} + 2w_{(k-2)N+3} - 8w_{(k-2)N+2} + w_{(k-3)N+2}$$

where we take the boundary conditions $w_{(k-1)N+2} + w_{(k-1)N} = 0$, here $w_{(k-1)N}$ is a virtual point, not the point in the N -th column.

Case2: point $p_{(k-1)N+3}$:

$$h^4 \nabla^4 w = w_{(k+1)N+3} + 2w_{kN+4} - 8w_{kN+3} + 2w_{kN+2} + w_{(k-1)N+5} - 8w_{(k-1)N+4} + 20w_{(k-1)N+3} - 8w_{(k-1)N+2} + 2w_{(k-2)N+4} - 8w_{(k-2)N+3} + 2w_{(k-2)N+2} + w_{(k-3)N+3}$$

where we take the boundary conditions $w_{(k-1)N+1} = 0$.

According to the symmetry, point $p_{(k-1)N+N-1}$ and point $p_{(k-1)N+N-2}$ are similar to the cases above.

Case3: point p_{N+m} where $4 \leq m \leq (N - 3)$:

$$h^4 \nabla^4 w = w_{(k+1)N+m} + 2w_{kN+m+1} - 8w_{kN+m} + 2w_{kN+m-1} + w_{(k-1)N+m+2} - 8w_{(k-1)N+m+1} + 20w_{(k-1)N+m} - 8w_{(k-1)N+m-1} + w_{(k-1)N+m-2} + 2w_{(k-2)N+m+1} - 8w_{(k-2)N+m} + 2w_{(k-2)N+m-1} + w_{(k-3)N+m}$$

So, we can conclude the general situation as a system of linear equations in matrix form as follows:

$$\mathbf{q}_k = I\mathbf{w}_{k+2} + A\mathbf{w}_{k+1} + B_{19}\mathbf{w}_k + A\mathbf{w}_{k-1} + I\mathbf{w}_{k-2}$$

After calculating the all three situations, we can get a final expression:

$$\frac{h^4}{D} \begin{bmatrix} \mathbf{q}_2 \\ \mathbf{q}_3 \\ \vdots \\ \mathbf{q}_{N-1} \end{bmatrix} = \begin{bmatrix} B_{18} & A & I & \mathbf{0} & \mathbf{0} & \cdots & \mathbf{0} & \mathbf{0} \\ A & B_{19} & A & I & \mathbf{0} & \cdots & \mathbf{0} & \mathbf{0} \\ I & A & B_{19} & A & I & \cdots & \mathbf{0} & \mathbf{0} \\ \vdots & \ddots & \ddots & \ddots & \ddots & \ddots & \vdots & \vdots \\ \vdots & \vdots & \ddots & \ddots & \ddots & \ddots & \vdots & \vdots \\ \mathbf{0} & \mathbf{0} & \cdots & I & A & B_{19} & A & I \\ \mathbf{0} & \mathbf{0} & \cdots & \mathbf{0} & I & A & B_{19} & A \\ \mathbf{0} & \mathbf{0} & \cdots & \mathbf{0} & \mathbf{0} & I & A & B_{18} \end{bmatrix} \cdot \begin{bmatrix} \mathbf{w}_2 \\ \mathbf{w}_3 \\ \vdots \\ \mathbf{w}_{N-1} \end{bmatrix}$$

Just solve this huge linear equation system, we can get all function values on the grid points and solve this partial difference equations.

As for the latter model, apply similar process on it, and denote different matrix:

$$B_{21} = \begin{pmatrix} 22 & -8 & 1 & 0 & 0 & \cdots & 0 & 0 \\ -8 & 21 & -8 & 1 & 0 & \cdots & 0 & 0 \\ 1 & -8 & 21 & -8 & 1 & \cdots & 0 & 0 \\ \vdots & \ddots & \ddots & \ddots & \ddots & \ddots & \vdots & \vdots \\ \vdots & \vdots & \ddots & \ddots & \ddots & \ddots & \vdots & \vdots \\ 0 & 0 & \cdots & 1 & -8 & 21 & -8 & 1 \\ 0 & 0 & \cdots & 0 & 1 & -8 & 21 & -8 \\ 0 & 0 & \cdots & 0 & 0 & 1 & -8 & 22 \end{pmatrix} \quad \text{and} \quad B_{20} = B_{21} - I$$

We can get similar huge linear equation system as

$$\frac{h^4}{D} \begin{bmatrix} \mathbf{q}_2 \\ \mathbf{q}_3 \\ \vdots \\ \mathbf{q}_{N-1} \end{bmatrix} = \begin{bmatrix} B_{21} & A & I & \mathbf{0} & \mathbf{0} & \cdots & \mathbf{0} & \mathbf{0} \\ A & B_{20} & A & I & \mathbf{0} & \cdots & \mathbf{0} & \mathbf{0} \\ I & A & B_{20} & A & I & \cdots & \mathbf{0} & \mathbf{0} \\ \vdots & \ddots & \ddots & \ddots & \ddots & \ddots & \vdots & \vdots \\ \vdots & \vdots & \ddots & \ddots & \ddots & \ddots & \vdots & \vdots \\ \mathbf{0} & \mathbf{0} & \cdots & I & A & B_{20} & A & I \\ \mathbf{0} & \mathbf{0} & \cdots & \mathbf{0} & I & A & B_{20} & A \\ \mathbf{0} & \mathbf{0} & \cdots & \mathbf{0} & \mathbf{0} & I & A & B_{21} \end{bmatrix} \cdot \begin{bmatrix} \mathbf{w}_2 \\ \mathbf{w}_3 \\ \vdots \\ \mathbf{w}_{N-1} \end{bmatrix}$$

3.2 Finite Element Analysis

We would explain the main method of Finite Element Analysis on thick plates problem and FEA on thin plates is similar.

3.2.1 Finite Element Analysis for Thick plate

We also applied Finite Element Analysis on thick plates problem, where our objective is to determine the displacement at each nodal point by employing the finite element method. In the context of finite element analysis, the primary objective is to derive the stiffness matrix \mathbf{K} for each finite element cell. This matrix encapsulates the relationship between nodal displacements and applied forces within the element which can be described as $\mathbf{Ku} = \mathbf{F}$ serving as a fundamental component in the assembly of the global stiffness matrix for the entire structure. In the subsequent sections, we will introduce various elements and methodologies essential for the derivation of the stiffness matrix. This will include a detailed exposition of the finite element construction process, encompassing the formulation of shape functions, the integration of material properties, and the application of boundary conditions. By systematically developing these components, we aim to provide a comprehensive understanding of the finite element method, facilitating its application to complex structural analyses. Katsikadelis [2014]

Now we build the specific finite element model. The middle plane of the plate is discretized into a finite element mesh comprising n -node elements. For illustrative purposes, Figure 4 depicts a discretization scheme utilizing 4-noded rectangular elements. This mesh structure serves as the foundation for the finite element analysis, enabling a detailed representation of the plate's geometry and facilitating the accurate computation of displacement, stress, and strain distributions within the material. Mukhopadhyay and Sheikh [2022]

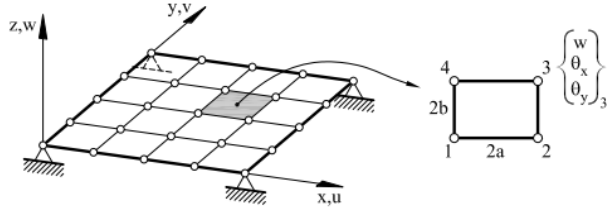


Figure 4: Discretization of a plate using 4-noded Reissner-Mindlin rectangles

From the Figure 4 we can see that each cell contains four nodes. And since each node has three degrees of freedom, we can get the displacement vector for each node, which we denote as $\mathbf{u}_i^{(e)}$, which is

$$\mathbf{u}_i^{(e)} = \{w_i, \theta_{x_i}, \theta_{y_i}\} \quad (3-2-1)$$

In the context of finite element analysis, we introduce the concept of shape functions to facilitate the interpolation of nodal variables within each element. In this study, we employ a novel shape function specifically designed for four-noded elements. The deflection and the two rotations are independent variables and the displacement field is interpolated in the standard C^0 form. Consequently, we can now explicitly formulate the expression for the displacement variable within the finite element framework.

$$\mathbf{u} = \begin{Bmatrix} w \\ \theta_x \\ \theta_y \end{Bmatrix} = \sum_{i=1}^n \begin{Bmatrix} N_i w_i \\ N_i \theta_{x_i} \\ N_i \theta_{y_i} \end{Bmatrix} = \begin{bmatrix} N_1 & 0 & 0 & \vdots & \vdots & N_n & 0 & 0 \\ 0 & N_1 & 0 & \vdots & \dots & \vdots & N_n & 0 \\ 0 & 0 & N_1 & \vdots & \vdots & 0 & 0 & N_n \end{bmatrix} \begin{Bmatrix} w_1 \\ \theta_{x_1} \\ \theta_{y_1} \\ \vdots \\ \vdots \\ w_n \\ \theta_{x_n} \\ \theta_{y_n} \end{Bmatrix} = [\mathbf{N}_1, \mathbf{N}_2, \dots, \mathbf{N}_n] \begin{Bmatrix} \mathbf{u}_1^{(e)} \\ \vdots \\ \mathbf{u}_n^{(e)} \end{Bmatrix} \quad (3-2-2)$$

where

$$\mathbf{N}_i = \begin{bmatrix} N_i & 0 & 0 \\ 0 & N_i & 0 \\ 0 & 0 & N_i \end{bmatrix}, \quad \mathbf{u}_i^{(e)} = \begin{Bmatrix} w_i \\ \theta_{x_i} \\ \theta_{y_i} \end{Bmatrix} \quad (3-2-3)$$

and to facilitate subsequent derivations, we further simplify the equation and streamlining the formulation for greater clarity into:

$$\mathbf{u} = \mathbf{N} \mathbf{u}^{(e)} \quad \text{where} \quad \mathbf{N} = [\mathbf{N}_1, \mathbf{N}_2, \dots, \mathbf{N}_n], \quad \mathbf{u}^{(e)} = \begin{Bmatrix} \mathbf{u}_1^{(e)} \\ \mathbf{u}_2^{(e)} \\ \vdots \\ \mathbf{u}_n^{(e)} \end{Bmatrix} \quad (3-2-4)$$

Then we can derive the generalized strain components, which are expressed as functions of the nodal displacements according to the Eq 2-2-3, Eq 3-2-2 and Eq 3-2-4:

$$\begin{aligned}\hat{\boldsymbol{\varepsilon}} &= \begin{Bmatrix} \hat{\varepsilon}_b \\ \dots \\ \hat{\varepsilon}_s \end{Bmatrix} = \begin{Bmatrix} \frac{\partial \theta_x}{\partial x} \\ \frac{\partial \theta_y}{\partial y} \\ \dots \\ \left(\frac{\partial \theta_x}{\partial y} + \frac{\partial \theta_y}{\partial x} \right) \\ \frac{\partial w}{\partial x} - \theta_x \\ \frac{\partial w}{\partial y} - \theta_y \end{Bmatrix} = \sum_{i=1}^n \begin{Bmatrix} \frac{\partial N_i}{\partial x} \theta_{x_i} \\ \frac{\partial N_i}{\partial y} \theta_{y_i} \\ \dots \\ \left(\frac{\partial N_i}{\partial y} \theta_{x_i} + \frac{\partial N_i}{\partial x} \theta_{y_i} \right) \\ \frac{\partial N_i}{\partial x} w_i - N_i \theta_{x_i} \\ \frac{\partial N_i}{\partial y} w_i - N_i \theta_{y_i} \end{Bmatrix} \\ &= \begin{Bmatrix} 0 & \frac{\partial N_i}{\partial x} & 0 \\ 0 & 0 & \frac{\partial N_i}{\partial y} \\ 0 & \frac{\partial N_i}{\partial x} & \frac{\partial N_i}{\partial y} \\ \dots & \dots & \dots \\ \frac{\partial N_i}{\partial x} & -N_i & 0 \\ \frac{\partial N_i}{\partial y} & 0 & -N_i \end{Bmatrix} \begin{Bmatrix} w_i \\ \theta_{x_i} \\ \theta_{y_i} \end{Bmatrix} = \sum_{i=1}^n \begin{Bmatrix} \mathbf{B}_{b_i} \\ \mathbf{B}_{s_i} \end{Bmatrix} \mathbf{u}_i^{(e)} \quad (3-2-5) \\ &= [\mathbf{B}_1, \dots, \mathbf{B}_n] \begin{Bmatrix} \mathbf{u}_1^{(e)} \\ \vdots \\ \mathbf{u}_n^{(e)} \end{Bmatrix} = \mathbf{B} \mathbf{u}^{(e)}\end{aligned}$$

where \mathbf{B} and \mathbf{B}_i are the generalized strain matrices for the element and a node i , respectively we deduce them as:

$$\mathbf{B}_i = \begin{Bmatrix} \mathbf{B}_{b_i} \\ \dots \\ \mathbf{B}_{s_i} \end{Bmatrix} \quad \text{with} \quad \mathbf{B}_{b_i} = \begin{bmatrix} 0 & \frac{\partial N_i}{\partial x} & 0 \\ 0 & 0 & \frac{\partial N_i}{\partial y} \\ 0 & \frac{\partial N_i}{\partial x} & \frac{\partial N_i}{\partial y} \end{bmatrix} \quad \text{and} \quad \mathbf{B}_{s_i} = \begin{bmatrix} \frac{\partial N_i}{\partial x} & -N_i & 0 \\ \frac{\partial N_i}{\partial y} & 0 & -N_i \end{bmatrix} \quad (3-2-6)$$

where \mathbf{B}_{b_i} and \mathbf{B}_{s_i} are the bending and transverse shear strain matrices associated to the i -th node, respectively. The resultant stresses are expressed in terms of the nodal displacements using Eq 2-2-4 and Eq 2-2-7, we can get that:

$$\hat{\boldsymbol{\sigma}} = \mathbf{D} \mathbf{B} \mathbf{u}^{(e)} \quad \text{and} \quad \hat{\boldsymbol{\sigma}}_b = \mathbf{D}_b \mathbf{B}_{b_i} \mathbf{u}^{(e)} \quad \text{and} \quad \hat{\boldsymbol{\sigma}}_s = \mathbf{D}_s \mathbf{B}_{s_i} \mathbf{u}^{(e)} \quad (3-2-7)$$

with

$$\mathbf{B}_b = [\mathbf{B}_{b_1}, \mathbf{B}_{b_2}, \dots, \mathbf{B}_{b_n}] \quad , \quad \mathbf{B}_s = [\mathbf{B}_{s_1}, \mathbf{B}_{s_2}, \dots, \mathbf{B}_{s_n}]$$

To facilitate the derivation of the stiffness matrix, we will employ the principle of virtual work. This principle is a fundamental concept in mechanics and structural analysis, which asserts that for a system in equilibrium, the virtual work done by internal and external forces during any virtual displacement is zero. Let us consider a plate loaded by a vertical distributed loads \mathbf{t} and point loads \mathbf{p}_i . The virtual work expression is written as:

$$\iiint_V \delta \boldsymbol{\varepsilon}^T \boldsymbol{\sigma} dV = \iint_A \delta \mathbf{u}^T \mathbf{t} dA + \sum_i \delta \mathbf{u}_i^T \mathbf{p}_i \quad (3-2-8)$$

where

$$\delta \mathbf{u} = [\delta w, \delta \theta_x, \delta \theta_y]^T \quad , \quad \mathbf{t} = [f_z, m_x, m_y]^T \quad , \quad \mathbf{p}_i = [P_{z_i}, M_{x_i}, M_{y_i}]^T$$

In the above equation, the left end of the left side of the equation: $\iiint_V \delta \boldsymbol{\varepsilon}^T \boldsymbol{\sigma} dV$ denotes the imaginary work done by all the internal forces within the plate volume V . Here $\delta \boldsymbol{\varepsilon}$ is the imaginary strain vector and $\boldsymbol{\sigma}$ is the stress tensor. At the right end of the equation, the first term at the right end: $\iint_A \delta \mathbf{u}^T \mathbf{t} dA$ denotes the imaginary work done by the external and distributed forces distributed on the plate surface A . Here $\delta \mathbf{u}$ is the imaginary displacement vector and \mathbf{t} is the surface load (which contains the components of the distributed load and distributed moment) and the second term at the right end: $\sum_i \delta \mathbf{u}_i^T \mathbf{p}_i$ denotes the imaginary work done by each of the centralised forces \mathbf{p}_i on the plate. Here $\delta \mathbf{u}_i$ is the imaginary displacement vector at the centralised loading point i . According to the Eq 2-2-7, we can replace \mathbf{V} and $\boldsymbol{\sigma}$ as follows:

$$\iiint_V \delta \boldsymbol{\varepsilon}^T \boldsymbol{\sigma} dV = \iint_A \delta \hat{\boldsymbol{\varepsilon}}^T \left[\int_{-t/2}^{t/2} \mathbf{S}^T \boldsymbol{\sigma} dz \right] dA = \iint_A \delta \hat{\boldsymbol{\varepsilon}}^T \hat{\boldsymbol{\sigma}} dA \quad (3-2-9)$$

The PVW is finally written in terms of integrals over the plate surface as:

$$\iint_A \delta \hat{\varepsilon}^T \hat{\sigma}^T dA = \iint_A \delta \mathbf{u}^T \mathbf{t} dA + \sum_i \delta \mathbf{u}_i^T \mathbf{p}_i \quad (3-2-10)$$

Now we continue to derive the stiffness matrix based on the previous variables and the PVW for a single element under distributed loads reads:

$$\iint_{A^{(e)}} \delta \hat{\varepsilon}^T \hat{\sigma} dA = \iint_{A^{(e)}} \delta \mathbf{u}^T \mathbf{t} dA + [\delta \mathbf{u}^{(e)}]^T \mathbf{q}^{(e)} \quad (3-2-11)$$

where $\delta \mathbf{u}^{(e)}$ is the virtual nodal displacement vector and the last term of the r.h.s. is the virtual work of the equilibrating nodal forces $\mathbf{q}^{(e)}$ with

$$\delta \mathbf{a}^{(e)} = \begin{Bmatrix} \delta \mathbf{a}_1^{(e)} \\ \vdots \\ \delta \mathbf{a}_n^{(e)} \end{Bmatrix}, \delta \mathbf{a}_i^{(e)} = \begin{Bmatrix} \delta w_i \\ \delta \theta_{x_i} \\ \delta \theta_{y_i} \end{Bmatrix}, \mathbf{q}^{(e)} = \begin{Bmatrix} \mathbf{q}_1^{(e)} \\ \vdots \\ \mathbf{q}_n^{(e)} \end{Bmatrix}, \mathbf{q}_i^{(e)} = \begin{Bmatrix} F_{z_i} \\ M_{x_i} \\ M_{y_i} \end{Bmatrix}$$

According to the Eq 3-2-4, Eq 3-2-5 and Eq 3-2-7, we can get that

$$\begin{aligned} \text{Eq}(3-2-10) &\Rightarrow \iint_{A^{(e)}} \delta \hat{\varepsilon}^T \mathbf{D} \mathbf{B} u^{(e)} dA = \iint_{A^{(e)}} \delta u^T t dA + \delta u^T q^{(e)} \\ &\Rightarrow \iint_{A^{(e)}} B^T [\delta u]^T \mathbf{D} \mathbf{B} u^{(e)} dA = \iint_{A^{(e)}} N [\delta u]^T t dA + [\delta u]^T q^{(e)} \\ &\Rightarrow [\delta u]^T \iint_{A^{(e)}} B^T \mathbf{D} \mathbf{B} u^{(e)} dA = [\delta u]^T \iint_{A^{(e)}} N t dA + [\delta u]^T q^{(e)} \\ &\Rightarrow \iint_{A^{(e)}} B^T \mathbf{D} \mathbf{B} dA \cdot u^{(e)} - \iint_{A^{(e)}} N t dA = q^{(e)} \\ &\Rightarrow \mathbf{K}^{(e)} \mathbf{u}^{(e)} - \mathbf{f}^{(e)} = \mathbf{q}^{(e)} \end{aligned} \quad (3-2-12)$$

where

$$\mathbf{K}_{ij}^{(e)} = \iint_{A^{(e)}} \mathbf{B}_i^T \mathbf{D} \mathbf{B}_j dA \quad \mathbf{f}_i^{(e)} = \iint_{A^{(e)}} \mathbf{N}_i [f_z, m_x, m_y]^T dA$$

Above all we derive an expression for the stiffness matrix in finite elements method and the element stiffness matrix can be split into the bending and transverse shear contributions as:

$$\mathbf{K}_{ij}^{(e)} = \iint_{A^{(e)}} [\mathbf{B}_{b_i}^T, \mathbf{B}_{s_i}^T]^T \mathbf{D} \begin{Bmatrix} \mathbf{B}_{b_j} \\ \mathbf{B}_{s_j} \end{Bmatrix} dA = \iint_{A^{(e)}} (\mathbf{B}_{b_i}^T \mathbf{D}_b \mathbf{B}_{b_j} + \mathbf{B}_{s_i}^T \mathbf{D}_s \mathbf{B}_{s_j}) dA = \mathbf{K}_{b_{ij}}^{(e)} + \mathbf{K}_{s_{ij}}^{(e)} \quad (3-2-13)$$

In subsequent finite element calculations, it was observed that directly using the above expression for the stiffness matrix $K^{(e)}$ is indeed more complex and computationally demanding. To address these issues, we employ a dual approach: converting from physical units to isoparametric units to standardize numerical integration and shape function evaluation, and simplifying the double integration process using the Gaussian integration method. This transformation to isoparametric units allows for a unified and efficient application of numerical integration techniques, while Gaussian quadrature significantly reduces the computational effort required for evaluating integrals, thereby enhancing overall computational efficiency and accuracy.

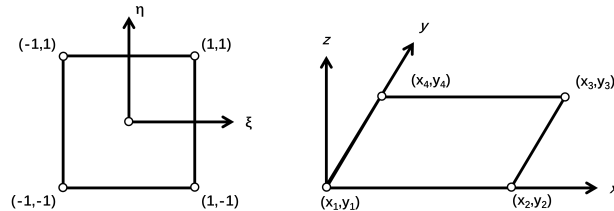


Figure 5: Coordinate system under the isoparametric unit and the Coordinate system under the physical unit

To streamline our finite element calculations, we first introduce the concept of the isoparametric unit. This concept is depicted in the accompanying figure, where the coordinate system under the physical unit is shown on the right, and the coordinate system under the isoparametric unit is on the left.

By converting from physical units to isoparametric units, we standardize the integration domain, allowing the use of a common set of shape functions and integration schemes across different element types. The shape function under the isoparametric cell is

$$\begin{aligned} N_1(\xi, \eta) &= \frac{1}{4}(1-\xi)(1-\eta) & N_2(\xi, \eta) &= \frac{1}{4}(1+\xi)(1-\eta) \\ N_3(\xi, \eta) &= \frac{1}{4}(1+\xi)(1+\eta) & N_4(\xi, \eta) &= \frac{1}{4}(1-\xi)(1+\eta) \end{aligned}$$

Due to the transformation of the coordinate system, the \mathbf{K} matrix undergoes coordinate mapping, partial derivative mapping, and area mapping. According to Eq 3-2-12, the resulting \mathbf{K} stiffness matrix is obtained under the isoparametric element formulation. Now we can get that:

$$\begin{aligned} x(\xi, \eta) &= N_1(\xi, \eta)x_1 + N_2(\xi, \eta)x_2 + N_3(\xi, \eta)x_3 + N_4(\xi, \eta)x_4 \\ y(\xi, \eta) &= N_1(\xi, \eta)y_1 + N_2(\xi, \eta)y_2 + N_3(\xi, \eta)y_3 + N_4(\xi, \eta)y_4 \end{aligned} \quad (3-2-14)$$

Above all, We can transform the equation into an isoparametric units form as:

$$\begin{aligned} \mathbf{K}_{ij}^{(e)} &= \iint_{A^{(e)}} (\mathbf{B}_{b_i}^T \mathbf{D}_b \mathbf{B}_{b_j} + \mathbf{B}_{s_i}^T \mathbf{D}_s \mathbf{B}_{s_j}) dA \\ &= \iint_{A^{(e)}} \mathbf{B}_{b_i}^T \mathbf{D}_b \mathbf{B}_{b_j} dA + \iint_{A^{(e)}} \mathbf{B}_{s_i}^T \mathbf{D}_s \mathbf{B}_{s_j} dA \\ &= \int_{-1}^1 \int_{-1}^1 \mathbf{B}_{b_i}^T \mathbf{D}_b \mathbf{B}_{b_j} \det(\mathbf{J}) d\xi d\eta + \int_{-1}^1 \int_{-1}^1 \mathbf{B}_{s_i}^T \mathbf{D}_s \mathbf{B}_{s_j} \det(\mathbf{J}) d\xi d\eta \end{aligned} \quad (3-2-15)$$

where $[J]$ we can get by chain rules as:

$$\begin{bmatrix} \frac{\partial f}{\partial \xi} \\ \frac{\partial f}{\partial \eta} \end{bmatrix} = \begin{bmatrix} \frac{\partial x}{\partial \xi} & \frac{\partial y}{\partial \xi} \\ \frac{\partial x}{\partial \eta} & \frac{\partial y}{\partial \eta} \end{bmatrix} \begin{bmatrix} \frac{\partial f}{\partial x} \\ \frac{\partial f}{\partial y} \end{bmatrix} = \begin{bmatrix} \frac{\partial N_1}{\partial \xi} & \frac{\partial N_2}{\partial \xi} & \frac{\partial N_3}{\partial \xi} & \frac{\partial N_4}{\partial \xi} \\ \frac{\partial N_1}{\partial \eta} & \frac{\partial N_2}{\partial \eta} & \frac{\partial N_3}{\partial \eta} & \frac{\partial N_4}{\partial \eta} \end{bmatrix} \begin{bmatrix} x_1 & y_1 \\ x_2 & y_2 \\ x_3 & y_3 \\ x_4 & y_4 \end{bmatrix} \begin{bmatrix} \frac{\partial f}{\partial x} \\ \frac{\partial f}{\partial y} \end{bmatrix} = [J] \begin{bmatrix} \frac{\partial f}{\partial x} \\ \frac{\partial f}{\partial y} \end{bmatrix}$$

Finally, we further simplify the double integration in the above equation by utilizing Gaussian quadrature. Gaussian integration is an efficient method for numerically approximating specific types of integrals. The core principle of Gaussian integration lies in the precise selection of a set of integration points and the corresponding weights, so that the weighted sum of the function values at these integration points can approximate the true value of the integral.

Gaussian quadrature achieves this by choosing integration points (often called Gauss points) and weights based on the roots of orthogonal polynomials, such as Legendre polynomials. These points and weights are specifically designed to provide the highest possible accuracy for polynomials of a given degree.

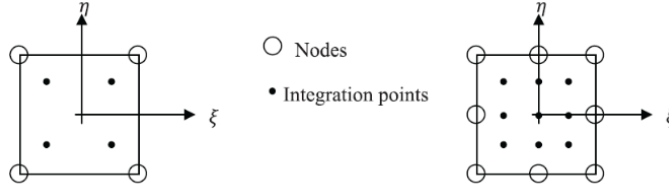


Figure 6: Gauss integration points for integrating. Figure on the left is 4 node isoparametric elements and Figure on the right is 8 node isoparametric elements

The 4-point Gaussian quadrature method, which is utilized in this algorithm, involves evaluating the integrand at four specific points within the element as 4 node isoparametric elements $\xi, \eta \in \{\frac{1}{\sqrt{3}}, -\frac{1}{\sqrt{3}}\}$ with the weight factors $w_i = w_j = 1$. According to the formula for the Gaussian integral, we have

$$\int_a^b f(x) dx \approx \sum_{i=1}^n w_i f(x_i) \quad (3-2-16)$$

Based on the Gaussian integration method (Eq 3-2-16) we can express Eq 3-2-15 into:

$$\begin{aligned} \mathbf{K}_{ij}^{(e)} &= \int_{-1}^1 \int_{-1}^1 \mathbf{B}_{b_i}^T \mathbf{D}_b \mathbf{B}_{b_j} \det(\mathbf{J}) d\xi d\eta + \int_{-1}^1 \int_{-1}^1 \mathbf{B}_{s_i}^T \mathbf{D}_s \mathbf{B}_{s_j} \det(\mathbf{J}) d\xi d\eta \\ &= \sum_{k=1}^2 \sum_{l=1}^2 w_k w_l ([\mathbf{B}_{b_i}(\xi_k, \eta_l)]^T [\mathbf{D}_b] [\mathbf{B}_{b_j}(\xi_k, \eta_l)] + [\mathbf{B}_{s_i}(\xi_k, \eta_l)]^T [\mathbf{D}_s] [\mathbf{B}_{s_j}(\xi_k, \eta_l)]) \det[\mathbf{J}(\xi_k, \eta_l)] \end{aligned} \quad (3-2-17)$$

In summary, we derive a specific expression for the K-matrix and simplify it further to reduce the complexity in the procedure. Based on this, we can use the finite element equation $\mathbf{K}\mathbf{u} = \mathbf{f}$ to solve for the unknown variable \mathbf{u} . By solving the equations, we are able to determine the deflection w_i at each node and the two corners θ_{xi} and θ_{yi} at the nodes.

3.2.2 Finite Element Analysis For Thin Plates

For the thin plate structure, since it does not contain shear strain, the component related to shear strain will be zero in the derivation of the finite element stiffness matrix, thus simplifying the expression of the stiffness matrix. Therefore, based on our derivation of the above equation (Eq 3-2-15 and Eq 3-2-17) we can derive the stiffness matrix in thin plates as follows:

$$\mathbf{K}_{ij}^{(e)} = \iint_{A^{(e)}} \mathbf{B}_{bi}^T \mathbf{D}_b \mathbf{B}_{bj} dA = \sum_{k=1}^2 \sum_{l=1}^2 w_k w_l [\mathbf{B}_{bi}(\xi_k, \eta_l)]^T [\mathbf{D}_b] [\mathbf{B}_{bj}(\xi_k, \eta_l)] \det[\mathbf{J}(\xi_k, \eta_l)] \quad (3-2-18)$$

Similarly based on the above \mathbf{K} through $\mathbf{K}\mathbf{u} = \mathbf{f}$, we can also fit the deflection variation using the finite element method.

4 Experiments

4.1 Comparison between FDM, FEA and exact solution on thin plates

We select a set of common parameters: $E = 2.1 \times 10^{11}$, $h = 0.01$, $\gamma = 0.3$ and $q(x, y) = q_0 = 10^6$ and the boundary conditions are *ssss* and *cccc* we mentioned above. (2.3)

The calculation formula of error is Mean Squared Error:

$$MSE(w) = \sqrt{\frac{1}{N^2} \sum_{i=1}^{N^2} (w_i - \hat{w}_i)^2}$$

where w_i and \hat{w}_i denote the numerical solution and the analytical solution respectively.

As for *ssss* model, we get the analytical solution from Navier's method (Jaeger). The main method is to take double Fourier series to get the exact solution of deflection w , which is:

$$w(x, y) = \sum_{m=1}^{\infty} \sum_{n=1}^{\infty} A_{mn} \sin(m\pi x) \sin(n\pi y) \quad \text{where } A_{mn} = \frac{4 \int_0^1 \int_0^1 q(x, y) \sin(m\pi x) \sin(n\pi y) dx dy}{\pi^4 D(m^2 + n^2)^2}$$

As for *cccc* model, it's hard to find the analytical solution directly, so we simulate it through an industrial software "Solidworks" (Shan-shan and Pu-hui [2015]). We use simulation tools in the software, and the material property of the plate in set the same to our assumption above.

Since the strategy of grid division of the simulated results of *cccc* model from the software is that the edges of the grid use a triangle mesh and the rest is a square mesh, which is different from us, so we choose the most representative point, the center point, to analyze our results.

We calculate the center point (coordinate (0.5,0.5)) on the grid under *ssss* model and *cccc* model and compare them with related analytical solution. The results are shown in Table 1 below.

Table 1: Numerical solution of deflections under different boundary conditions on the center point of 128x128 grid

Methods	Boundary conditons	Coordinate	Calculated solution	Analytical solution	Relative error
FDM	ssss	(0.5,0.5)	2.11241e-01	2.11242e-01	1.0e-06
FEA	ssss	(0.5,0.5)	2.11236e-01	2.11242e-01	6.0e-06
FDM	cccc	(0.5,0.5)	6.58314e-02	6.57762e-02	5.5e-05
FEA	cccc	(0.5,0.5)	6.58047e-02	6.57762e-02	2.8e-05

Here, we take the relative error: $error = |w - \hat{w}|$ where w and \hat{w} represent for the numerical and analytical deflection on the center point respectively. Also, we conducted our experiments on different methods on *ssss* model under different grid density. The Figure 7 plotted is the result, where the Grid Parameter n represents for the $n \times n$ grid meshing:

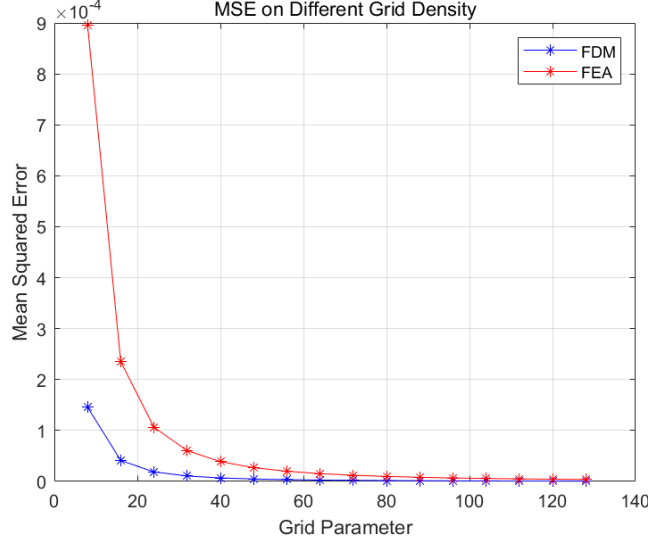


Figure 7: Relationship between MSE and grid density on $ssss$ model with two methods

From the Table 1 and Figure 7 above, we've learned that on solving the Kirchhoff thin plates problem, as the grid meshing becomes denser, the MSE of both FDM and FEA becomes smaller. The main difference is that the more sparsely the grid is divided, FEA shows little stability and FDM is relatively stable.

From the Figure 7, we discover that after about $n > 80$, the MSE of both methods stabilise and when n is relatively small, especially $0 < n < 30$, we saw a enormous magnitude of change.

In order to find out the reasons behind it, above all, we want to explore the effect of other parameters (e.g. thickness, property of materials). So, we first conduct other several experiments with changing the thickness: $h \in \{0.01, 0.03, 0.05, 0.07, 0.09\}$, $E = 2.1 \times 10^{11}$, $\gamma = 0.3$.

The second experiment is control the thickness, changing the material parameters: $(E, \gamma) \in \{(8.16 \times 10^{11}, 0.42), (1.155 \times 10^8, 0.34), (2.1 \times 10^{11}, 0.3)\}$ and $h = 0.01$, where the specific parameters come from some common material and the results are as follows:

From the Figures 8 and Figures 9 below, the situation that when n is relatively small, especially $0 < n < 30$, we saw a enormous magnitude of change still exists. Furthermore, as to FEA, it seems no direct relationships between the plate thickness h and the MSE. But as to FDM, we can find that there exists a trend that under the same meshing, thicker the plates, less the MSE, which means FDM will work better with denser grid meshing.

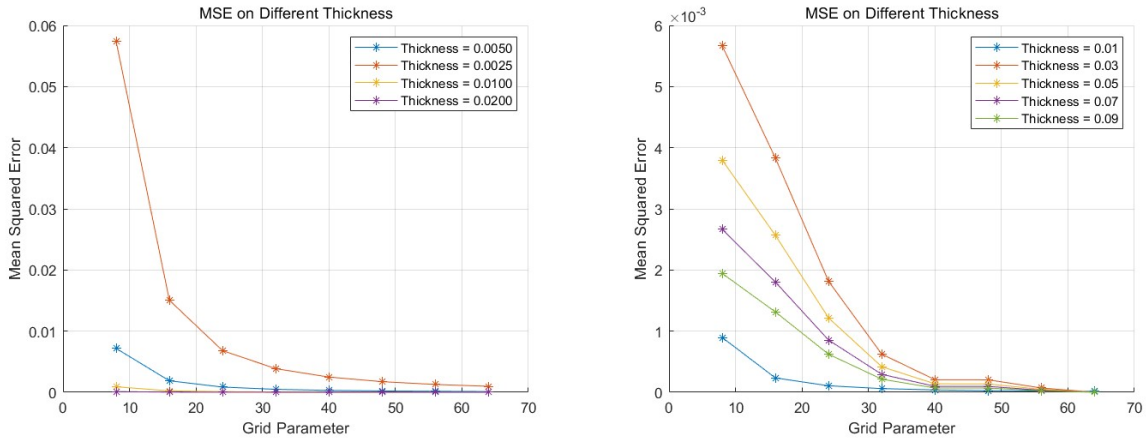
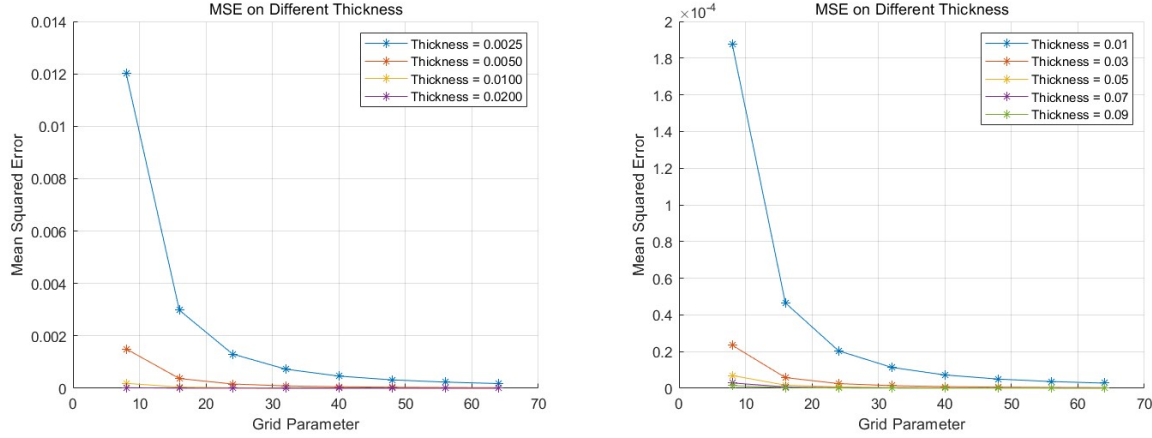
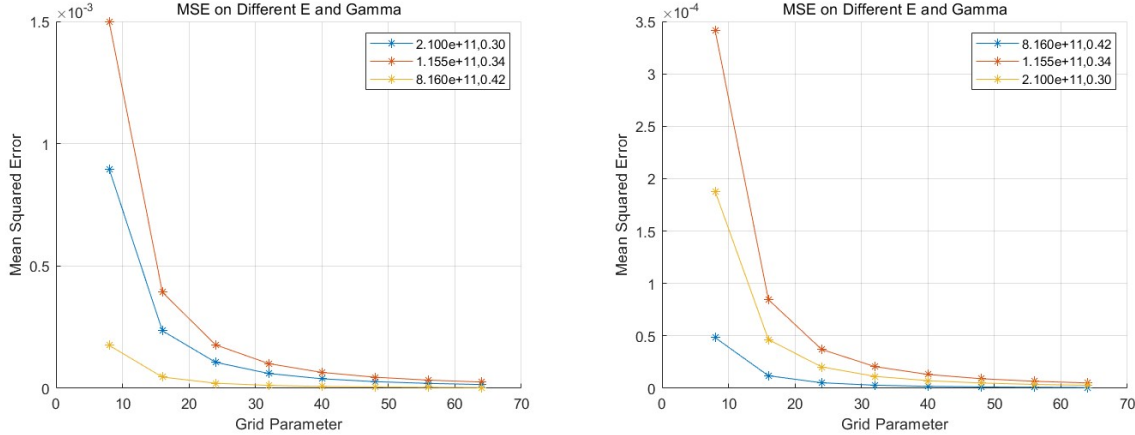


Figure 8: The results of changing thickness h through FEA


 Figure 9: The results of changing thickness h through FDM

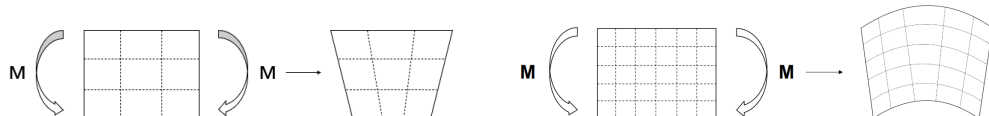
From the Figures 10 below, we cannot conclude from the figures about the relationship between some materials and related MSE. However, the special phenomenon we mentioned above still exists, which can be noted from the plunge of MSE in the curve from $n < 10$ to $n \geq 30$.


 Figure 10: The comparison of changing material parameter E and γ through FEA (left) and FDM (right) respectively

So then we mainly focus on this phenomenon called shear locking and have done some in-depth research about it.

4.2 Shear locking

In the experiment described above, we observed a notable phenomenon: under identical parameter conditions, gradually increasing the density of the finite element mesh resulted in displacement values that more accurately approximated the exact solution. This demonstrates that enhancing mesh density enables the finite element method (FEM) to produce computational results that more closely align with theoretical values. Conversely, as mesh density decreases, the error in the FEM solution becomes significantly larger. This error amplification is particularly pronounced in the analysis of thin plates, indicating that a reduction in plate thickness exacerbates the error. Shufrin and Eisenberger [2006]


 Figure 11: Linear cell deformation and Quadratic unit deformation of Fully integrated under bending moment M

To gain a deeper understanding of this phenomenon, we conducted further investigations. A comprehensive review of the related literature revealed that this occurrence is attributable to an intrinsic drawback of the finite element method known as shear locking. Specifically, when calculations are performed in finite element analysis using lower order cells, such as in linear cells, these cells have significant limitations in modelling shear deformation. Low-order units are unable to accurately capture the shear deformation characteristics of the structure under actual stress conditions, leading to an artificial overestimation of the shear stiffness during the calculation process.

Taking the plate structure as an example, when we use linear cells for finite element analysis, the edges of these cells remain straight before and after deformation because each edge of a linear cell consists of only two nodes. Specifically, when the plate is subjected to force bending, the upper surface is stretched while the lower surface is compressed, resulting in the neutral layer in the middle of the plate thickness no longer remaining straight, but undergoing shear deformation. This shear deformation is due to the inability of the linear cell to correctly represent the actual shear strain changes that occur during bending during the simulation. As a result, the shear deformation consumes part of the deformation energy, making the cell appear too stiff in the numerical simulation, and the amount of bending deformation is significantly reduced. Due to this inaccurate stiffness representation, a significant gap between the simulation results and the theoretically calculated values occurs.

On the other hand, we can also observe this phenomenon by means of the specific formulae in the above finite elements (Eq 3-2-15 and Eq 2-2-10), and the main problem arises in the stiffness matrix \mathbf{K} :

$$\begin{aligned}\mathbf{K}_{ij}^{(e)} &= \int_{-1}^1 \int_{-1}^1 \mathbf{B}_{bi}^T \mathbf{D}_b \mathbf{B}_{bj} \det(\mathbf{J}) d\xi d\eta + \int_{-1}^1 \int_{-1}^1 \mathbf{B}_{si}^T \mathbf{D}_s \mathbf{B}_{sj} \det(\mathbf{J}) d\xi d\eta \\ &= \frac{t^3}{12} \int_{-1}^1 \int_{-1}^1 \mathbf{B}_{bi}^T \hat{\mathbf{D}}_b \mathbf{B}_{bj} \det(\mathbf{J}) d\xi d\eta + t \int_{-1}^1 \int_{-1}^1 \mathbf{B}_{si}^T \hat{\mathbf{D}}_s \mathbf{B}_{sj} \det(\mathbf{J}) d\xi d\eta\end{aligned}\quad (4-2-1)$$

where

$$\mathbf{K}_{bi,j}^{(e)} = \frac{t^3}{12} \int_{-1}^1 \int_{-1}^1 \mathbf{B}_{bi}^T \hat{\mathbf{D}}_b \mathbf{B}_{bj} \det(\mathbf{J}) d\xi d\eta \quad \text{and} \quad \mathbf{K}_{si,j}^{(e)} = t \int_{-1}^1 \int_{-1}^1 \mathbf{B}_{si}^T \hat{\mathbf{D}}_s \mathbf{B}_{sj} \det(\mathbf{J}) d\xi d\eta$$

The matrix $\mathbf{K}_{bi,j}^{(e)}$ in the given equation represents the strain energy associated with in-plane stresses and strains, whereas $\mathbf{K}_{si,j}^{(e)}$ corresponds to the strain energy associated with out-of-plane shear stresses and shear strains. In subsequent computations, we employ the Gaussian integration method for numerical integration. Due to the presence of the thickness coefficient t in the equation, we observe that as the thickness of the plate decreases, the in-plane strain energy scales with the third power of the thickness as $\mathbf{K}_{bi,j}^{(e)} \propto t^3$, while the out-of-plane shear strain energy scales with the first power of the thickness as $\mathbf{K}_{si,j}^{(e)} \propto t$. Consequently, the stiffness term associated with out-of-plane shear stresses becomes significantly larger than the stiffness term associated with in-plane bending stresses. This disparity leads to an overestimation of the stiffness in the out-of-plane direction, resulting in an overly rigid numerical model for thin plates. In other words, as the plate thickness decreases, the contribution of in-plane strain energy decreases dramatically, while the effect of out-of-plane shear strain energy diminishes relatively less. This imbalance makes the stiffness term of the out-of-face shear stresses dominate the overall stiffness matrix, which leads to an excessively stiff out-of-face behaviour of the cells in the numerical simulations.

To mitigate the effects of shear locking, the method of reduced integration can be employed to a certain extent. Specifically, in the Gaussian integration process, consider a four-node rectangular element. Using full integration, as indicated in Eq 3-2-17, a total of four integration points are typically utilized. However, through the reduced integration method, only one integration point is used in each direction, resulting in a total of one integration point for the element.

$$\begin{aligned}\mathbf{K}_{ij}^{(e)} &= \int_{-1}^1 \int_{-1}^1 \mathbf{B}_{bi}^T \mathbf{D}_b \mathbf{B}_{bj} \det(\mathbf{J}) d\xi d\eta + \int_{-1}^1 \int_{-1}^1 \mathbf{B}_{si}^T \mathbf{D}_s \mathbf{B}_{sj} \det(\mathbf{J}) d\xi d\eta \\ &= w_\xi w_\eta [\mathbf{B}_{bi}(0,0)]^T [\mathbf{D}_b] [\mathbf{B}_{bj}(0,0)] \det[\mathbf{J}(0,0)] + w_\xi w_\eta [\mathbf{B}_{si}(0,0)]^T [\mathbf{D}_s] [\mathbf{B}_{sj}(0,0)] \det[\mathbf{J}(0,0)]\end{aligned}\quad (4-2-2)$$

This reduction in the number of integration points effectively diminishes the cumulative contribution to the shear strain energy during the computation. Consequently, it helps avoid the overestimation of shear strain energy, which is a common issue associated with full integration in the analysis of thin structures. The result obtained after the reduction of the integral is shown in Figure 12.

Although the MSE with reduced integration method when the Grid Parameter $n > 20$ becomes a bit larger than the origin method, when $n < 20$, we get a much more stable MSE, which means after we applied reduced integration method on the plates, the error come from shear-locking phenomenon can be almost corrected.

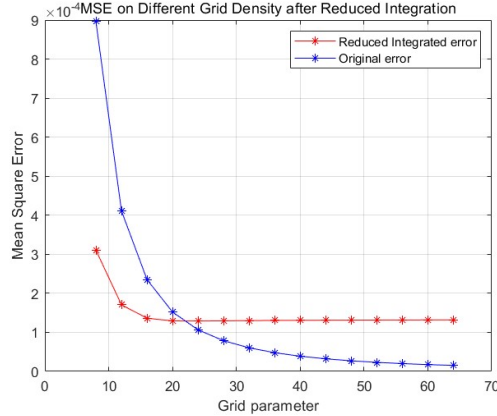


Figure 12: The comparison of MSE between Original Method and Reduced Integration Method under *cccc* condition

4.3 Comparison between deflections on thin and thick plates solving by FEA under the same load

From the Figures 13 below, the deflections of thin plates are almost generally greater than that of thick plates, which is in line with normal understanding.

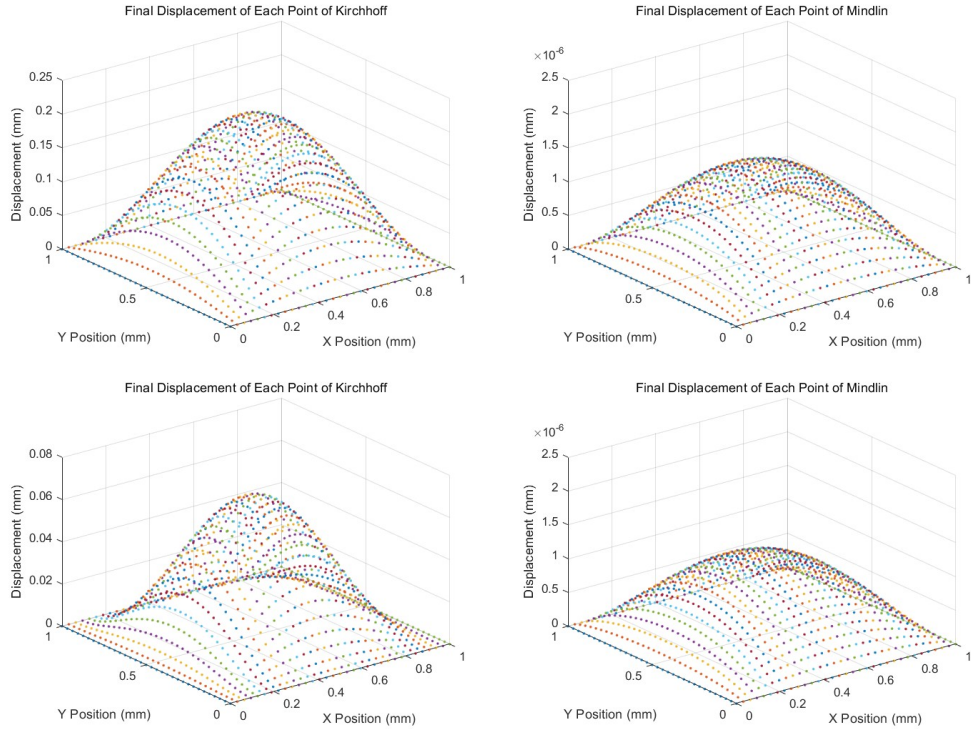


Figure 13: The comparison of thin and thick plates under *ssss* condition (top two) and *cccc* condition (bottom two)

Based on our speculation, reasons are as follows: since the flexural rigidity $D = \frac{Eh^3}{12(1-\nu^2)} \propto h^3$, with lower thickness in Kirchhoff plate, D becomes lower, and in Reissner-Mindlin thick plate, D becomes higher. Thus, under the same load, the deflection of the Kirchhoff plate is larger than the deflection of the Reissner-Mindlin thick plate.

Also, as to Kirchhoff thin plates, different boundary conditions would have a significant effect on deflection, but as to Reissner-Mindlin thick plates, different boundary conditions seem to have little effect on deflection. We guess that it may be caused by our parameter choice: E and the related flexural rigidity D and we would have in-depth research on it in future work.

5 Extension Research

5.1 Further study of shear locking

In the above section, in order to solve the shear self-locking problem, we use the reduced integration method. The reduced integration method reduces the stiffness of the stiffness matrix by reducing the number of integration points, so that the problem of excessive stiffness of the model can be alleviated. Specifically, the reduced integration method uses fewer integration points in the calculation process to reduce the shear locking effect brought about by numerical integration.

However, this method does increase the stability of the model to a certain extent and effectively mitigates the shear self-locking problem. However, this approach also brings certain negative effects as the error of the model increases. Due to the reduction in the number of integration points, the accuracy of the numerical integration decreases, which leads to an increase in the error of the overall simulation results.

After conducting a thorough discussion, we identified several alternative solutions that appear to be more effective. These solutions were evaluated based on empirical evidence and rigorous analysis.

On the one hand, we think that a simple and effective way to overcome shear locking is to use different finite element methods for different components of the stiffness array. Since the shear self-locking problem is due to an overestimation of the shear stiffness matrix, then in combination with our previous equations Eq 3-2-17 and Eq 4-2-2, we feel that we can use a four-node Gaussian integration method for the bending stiffness matrix calculations and a reduced integration, also known as a single-node Gaussian integration method, for the shear stiffness matrix. Thus we can specifically obtain the new formula

$$\begin{aligned} \mathbf{K}_{ij}^{(e)} &= \int_{-1}^1 \int_{-1}^1 \mathbf{B}_{bi}^T \mathbf{D}_b \mathbf{B}_{bj} \det(\mathbf{J}) d\xi d\eta + \int_{-1}^1 \int_{-1}^1 \mathbf{B}_{si}^T \mathbf{D}_s \mathbf{B}_{sj} \det(\mathbf{J}) d\xi d\eta \\ &= \sum_{k=1}^2 \sum_{l=1}^2 w_k w_l [\mathbf{B}_{bi}(\xi_k, \eta_l)]^T [\mathbf{D}_b] [\mathbf{B}_{bj}(\xi_k, \eta_l)] \det[\mathbf{J}(\xi_k, \eta_l)] \\ &\quad + w_\xi w_\eta [\mathbf{B}_{si}(0, 0)]^T [\mathbf{D}_s] [\mathbf{B}_{sj}(0, 0)] \det[\mathbf{J}(0, 0)] \end{aligned} \quad (5-1-1)$$

By using the above approach, we believe it possible to reduce the overestimation of the shear stiffness matrix on the one hand, and on the other hand to make the values more accurate and stable by increasing the number of integration points.

On the other hand, to address the issue of shear self-locking, we propose starting with the shape function. By employing higher-order shape functions, we can achieve a more detailed representation of deformation and thereby reduce numerical integration errors. Furthermore, higher-order shape functions offer a more accurate depiction of the actual physical behavior. Based on specific shape function, the displacement vector can be constructed as:

$$\begin{aligned} w = \sum_{i=1}^4 w_i \frac{1}{4} (1 + \xi_i \xi) (1 + \eta_i \eta) + w'_5 \frac{1}{2} (1 - \xi^2) (1 + \eta) + w'_6 \frac{1}{2} (1 - \eta^2) (1 - \xi) \\ + w'_7 \frac{1}{2} (1 - \xi^2) (1 - \eta) + w'_8 \frac{1}{2} (1 - \eta^2) (1 + \xi) \end{aligned} \quad (5-1-2)$$

where $w'_i (i = 5 \sim 8)$ can be expressed as $w_i, \theta_{x_i}, \theta_{y_i} (i = 1 \sim 4)$ and in order for the form function to satisfy the equilibrium differential equation at the corner points, we can finally get:

$$\begin{aligned} w = \sum_{i=1}^4 w_i \frac{1}{4} (1 + \xi_i \xi) (1 + \eta_i \eta) + \frac{l}{4} (\theta_{y_1} - \theta_{y_2}) \frac{1}{2} (1 - \xi^2) (1 + \eta) + \frac{l}{4} (\theta_{x_3} - \theta_{x_2}) \frac{1}{2} (1 - \eta^2) (1 - \xi) \\ + \frac{l}{4} (\theta_{y_4} - \theta_{y_3}) \frac{1}{2} (1 - \xi^2) (1 - \eta) + \frac{l}{4} (\theta_{x_4} - \theta_{x_1}) \frac{1}{2} (1 - \eta^2) (1 + \xi) \end{aligned} \quad (5-1-3)$$

By constructing the above higher order shape functions, we can construct a more accurate finite element model, through which the deflection variation of the plate can be better described on the one hand, and on the other hand, the equilibrium relationship inside the cell is improved and the equilibrium differential equations are directly satisfied. Of course, while trying to use the higher order shape functions to better describe the displacement of the plate, it is also necessary to maintain the degree of freedom of the nodes corresponding to the lower order shape functions. Through the two methods we have discussed above we have been able to improve the accuracy and reduce the shear self-locking phenomenon through theoretical calculations.

5.2 Modal analysis

Modal analysis has many uses in structural finite element simulation, the most direct role is to obtain the intrinsic frequency and vibration pattern of the model. Kishore et al. [2017] Saunders [2011]

Based on the intrinsic frequency, vibration pattern and excitation, it can be judged whether the model will resonate under a specific excitation. So we did some extra research on modal analysis of thin plates with *ssss* model and obtained the first 6 orders of the modal mode shapes:

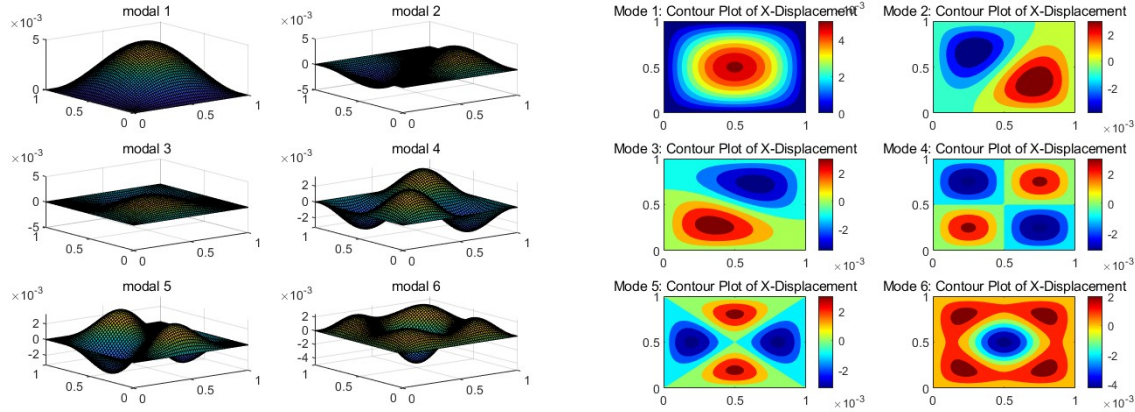


Figure 14: The modal of the Kirchhoff plate with modal number 6 and the contour of the modal

6 Conclusion

In this study, we began by physically modeling Kirchhoff thin plates and Reissner-Mindlin thick plates, exploring the deflection characteristics of both. To establish the relationship between the deflection and the applied load, we examined different research methodologies, specifically the Finite Difference Method (FDM) and Finite Element Analysis (FEA). We also adjusted boundary conditions, specifically *ssss* model and *cccc* model, to investigate their effects on deflection. According to Mean Squared Error (MSE), FDM performed relatively more stably than FEA, with both methods approximating an error close to 10^{-4} at high grid densities. Furthermore, we visualized the deflection of thin and thick plates under the same load and both *ssss* and *cccc* model.

During our experiments, we encountered the phenomenon of shear locking, a prevalent issue in the analysis of plate bending problems, especially when dealing with thin plates. To mitigate this problem, we employed the reduced integration method, a technique that involves using a lower order of integration to calculate the stiffness matrix. Furthermore, we conducted a preliminary modal analysis using finite element simulation and obtained the first six orders of modal mode shapes of thin plates with the *ssss* boundary condition. These results provide a foundational understanding of the dynamic behavior of thin plates and will serve as a basis for future research on more complex loading conditions and boundary constraints.

Our future research would focus on the following aspects: firstly, extending the modal analysis to include higher order modes and comparing the results with experimental data, which can help to improve the reliability of the computational models. In addition, investigating the effects of material properties and geometric nonlinearities on modal behaviour is also an important direction. Secondly, nonlinear analysis is explored, especially large deformation and plasticity effects. Studying the behaviour of plates under dynamic loading conditions, such as impact or cyclic loading, can provide insights into their performance and potential failure mechanisms. Another important direction is the application of optimisation techniques, whereby weight minimisation or stiffness maximisation of plate structures can be achieved through optimisation algorithms based on deformation and modal properties. Further research into alternative techniques for mitigating shear locking, such as higher order cells or hybrid methods, can improve simulation accuracy and efficiency. After that we can also continue to delve into plate and shell theory to understand the shell structure and make simulation models.

References

- Zhuochao Tang, Zhuo-Jia Fu, and Chia-Ming Fan. Generalized finite difference method for solving kirchhoff plate and winker plate bending problems. *Guti Lixue Xuebao/Acta Mechanica Solida Sinica*, 39:419–428, 08 2018. doi:10.19636/j.cnki.cjsm42-1250/o3.2018.005.
- A. MITCHELL and David Griffiths. *The Finite Difference Method in Partial Differential Equations*. 01 1980.
- Nazare Mayuresh Sudhir. Plate bending analysis using finite element method. 2012. URL <https://api.semanticscholar.org/CorpusID:107695850>.
- Eugenio Oñate. *Thin Plates. Kirchhoff Theory*, pages 233–290. Springer Netherlands, Dordrecht, 2013a. ISBN 978-1-4020-8743-1. doi:10.1007/978-1-4020-8743-1_5.
- Eugenio Oñate. *Thick/Thin Plates. Reissner-Mindlin Theory*, pages 291–381. Springer Netherlands, Dordrecht, 2013b. ISBN 978-1-4020-8743-1. doi:10.1007/978-1-4020-8743-1_6.
- Yan Shang, Song Cen, Chen-Feng Li, and Xiang-Rong Fu. Two generalized conforming quadrilateral mindlin–reissner plate elements based on the displacement function. *Finite Elements in Analysis and Design*, 99:24–38, 2015. ISSN 0168-874X. doi:<https://doi.org/10.1016/j.finel.2015.01.012>.
- John T. Katsikadelis. Chapter two - bem for plate bending analysis. In John T. Katsikadelis, editor, *The Boundary Element Method for Plate Analysis*, pages 21–111. Academic Press, Oxford, 2014. ISBN 978-0-12-416739-1. doi:<https://doi.org/10.1016/B978-0-12-416739-1.00002-0>.
- Madhujit Mukhopadhyay and Abdul Hamid Sheikh. *Finite Element Analysis of Plate Bending Problems*, pages 235–285. Springer International Publishing, Cham, 2022. ISBN 978-3-031-08724-0. doi:10.1007/978-3-031-08724-0_11.
- L.G. Jaeger. Chapter ii - the rectangular plate under transverse loading. navier's method. In *Elementary Theory of Elastic Plates*, The Commonwealth and International Library: Structures and Solid Body Mechanics Division. doi:<https://doi.org/10.1016/B978-0-08-010342-6.50005-0>. URL <https://www.sciencedirect.com/science/article/pii/B9780080103426500050>.
- XIAO Shan-shan and CHEN Pu-hui. Analytical solutions for bending of clamped orthotropic rectangular plates under a concentrated force. *Engineering Mechanics*, 32(6):28–32, 2015. ISSN 1000-4750. doi:10.6052/j.issn.1000-4750.2013.12.1178.
- Igor Shufrin and Moshe Eisenberger. Shear buckling of thin plates with constant in-plane stresses. In C. A. Motasoares, J. A. C. Martins, H. C. Rodrigues, Jorge A. C. Ambrósio, C. A. B. Pina, C. M. Motasoares, E. B. R. Pereira, and J. Folgado, editors, *III European Conference on Computational Mechanics*, pages 704–704, Dordrecht, 2006. Springer Netherlands.
- M.L. Pavan Kishore, Sreenivasulu Bezwada, and B.C. Raghu Kumar Reddy. Modal analysis of rectangular plate with central hole subjected to various end conditions. *Materials Today: Proceedings*, 4(2, Part A):1653–1661, 2017. ISSN 2214-7853. doi:<https://doi.org/10.1016/j.matpr.2017.02.004>. 5th International Conference of Materials Processing and Characterization (ICMPC 2016).
- Wesley Saunders. Modal analysis of rectangular simply-supported functional graded plates. 2011. URL <https://api.semanticscholar.org/CorpusID:126302739>.